Morelos-Pacheco *et al.*
Phytopathology Research (2025) 7:36
https://doi.org/10.1186/s42483-025-00323-7

Phytopathology Research

RESEARCH

Open Access

Fabrication of a plasmonic-nose sensor for rapid identification of plant pathogenic bacteria based on optoelectronic analysis

Mariela Morelos-Pacheco[1], Marco A. Arellano-Alcántara[1], Jonatan Olivares-Peralta[1], Raul Colmenero-Solís[1], José M. Saniger-Blesa[2], Juan C. Cancino-Díaz[3], Joakim Widén[4], Belén Chávez-Ramírez[5] and José Silvestre Mendoza-Figueroa[1*]

Abstract

Plant pathogenic bacteria are one of the most important threats to agriculture production, diminishing the growth and development of host crops. Bacterial diagnostic is based on traditional microbiological methods, including isolation, purification, and a further confirmatory immunological or molecular test for accurate identification. In this work, we present the design and fabrication of a plasmonic optoelectronic sensor based on seven "olfactory receptors" formed by seven gold nanoparticle (AuNP) morphologies, including nano bones, nanospheres, nanorods, and nano shuttles with two sizes and nanostars. The AuNPs work as a central part of the sensor for color change analysis, the principle of which is based on the reduction of Tollens' reagent with aldehydes produced by the tested phytopathogenic bacteria during their growth. Depending on the concentration and redox potential of the produced aldehydes, the reduction of Tollens' reagent will be a critical step in differentiating between bacteria species. A photograph captures the colorimetric response, and then the RGB values are extracted with an image analysis algorithm designed and presented here. Our results show clear chemical discrimination between five plant pathogenic bacteria after 3 h of incubation in the sensor; no misclassification was observed after this incubation time using hierarchical cluster analysis and linear discrimination analysis. In an experimental model, the sensor correctly classified *Pseudomonas savastanoi* pv. *phaseolicola* isolated from halo blight symptomatic leaves and distinguished between other fluorescent bacteria isolated from bean leaves. In addition, the image analysis algorithm presented here can improve RGB extraction due to removing interferences in the sensor substrate compared with the already reported RGB color extraction methods.

Keywords AuNPs, Plasmonic nose, Plant pathogenic bacteria, Optoelectronic, Chemometric, Aldehyde, Tollens

*Correspondence:
José Silvestre Mendoza-Figueroa
jmendozafi@ipn.mx
Full list of author information is available at the end of the article

Background

Plant pathogenic bacteria are one of the most devastating etiological agents of crops worldwide; bacterial diseases can cause symptoms in host plants like blights, fire blight, wilting, crown galls, soft rot, and oxidative stress (Nazarov et al 2020; Ma et al. 2022). Mansfield et al. (2012) proposed a top 10 list of the most important plant pathogenic bacteria from the scientific and economic impact point of view. This list included species like *Pseudomonas syringae* pathovares, *Ralstonia solanacearum*, *Agrobacterium tumefanciens*, different species of *Xanthomonas*, *Erwinia amylovora*, *Xyllela fastidiosa*, *Dickeya*, and *Pectobacterium carotovorum*, with also special mention to *Clavibacter michiganensis*, *Pseudomonas savastanoi*, and *Candidatus* Liberibacter asiaticus. The traditional methods for diagnosing a bacterial disease include the observation of symptoms, microbiological tests, immunological assays, and molecular methods like PCR (Venbrux et al. 2023). Recently, biosensors and chemosensors have been presented as an alternative for the detection of plant pathogens in a short time without high-cost instruments (Cardoso et al. 2022). Chemosensors consist of a chemical recognition element for sensing an analyte. This chemical recognition element can produce a detectable signal or can be combined with a physicochemical or electronic transducer to produce a measurable signal after the chemical reaction (Krämer et al. 2022). If the chemosensor is combined with an optical and digital analysis, it is named an optoelectronic sensor (Bordbar et al. 2020a, b). In chemosensors, some promising recognition elements are gold nanoparticles (AuNPs) due to their physicochemical properties depending on size, shape, and composition. It is well known that anisotropic nanoparticles can improve the sensitivity in sensing devices because of their high refraction index and refraction index sensitivity (Chen et al. 2008; Tuersun et al. 2017). In this work, we present a chemosensor based on gold nanoparticles forming a chemical nose formed by seven "olfactory receptors" (seven AuNPs morphologies) for the classification of plant pathogenic bacteria. The sensor is coupled to an optoelectronic analysis through an image analysis algorithm to extract the RGB pattern for further chemometric classification analysis. Bacteria can produce volatile organic compounds (VOCs) during the growth metabolism. The main VOCs are small-chain organic acids, alcohols, ketones, and aldehydes. Recent reports have shown the fabrication of sensors for the detection of volatile aldehydes using gold nanoparticles. Those sensors use the reduction power of the aldehyde on a chemical compound containing silver (Tollen´s reagent) for modifying the localized surface plasmon resonance (LSPR) on the AuNPs (sensor element), with a consequent silver deposition around the nanoparticle (Zhang et al. 2021). In this work, we use both principles to design a plasmonic nose containing AuNPs as a sensor element embedded in a polymeric matrix in an alkaline environment given by Tollens´ reagent to react with volatile aldehydes produced during bacterial metabolism. It is also known that alpha-hydroxy ketones can react with Tollen´s reagent because alpha-hydroxy ketones can tautomerize to aldehydes (Liao et al. 2021). It has been reported that during the bacterial primary metabolism, some aldehydes can be produced by microorganisms such as 3-methylbutanal, butanal, mercaptopropanal, nonanal, and alpha-hydroxy ketones such as acetoin (Weisskopf et al. 2021). These example molecules could be sensed by the plasmonic sensor presented here, and according to the concentration and production of a specific bacteria species, they will give a different chemical classification pattern.

Results

Gold nanoparticle synthesis

The Fig. 1a, b show the TEM micrographs of AuNPs used for sensor fabrication and the characteristic plasmon curves, respectively. The gold nanobones (GNB) of average size of 60 nm (Fig. 1a–i, b–i) show two plasmon peaks corresponding to longitudinal plasmon (700 nm), and transversal plasmon derived from edges in the broad and constricted part of the bone-like structure located between 500 and 600 nm. Gold nanospheres (GNSph) (Fig. 1a-ii, b-ii) of the average size of 30 nm exhibit a unique plasmon peak at 530 nm corresponding to the isotropic morphology. Two nanorod sizes were synthesized with the average size in the longitudinal face of 50 nm (Fig. 1a-iii) and 62 nm (Fig. 1a-iv) with a longitudinal plasmon peak at 680 nm (Fig. 1b-iii) and 700 nm (Fig. 1b-iv), respectively. These nanorod particles were used as seeds for synthesizing nano shuttles (GNSht) (Fig. 1a-v, vi) showing a modification in the intensity of the transverse plasmon mode due to the widening of nanorod tips (Fig. 1b-v, vi). Finally, gold nanostars (GNStr) showed a dispersed size (Fig. 1a-vii), and the plasmon curves show a broad spectrum from 500 to 800 nm (Fig. 1b-vii) due to central spherical morphology and the presence of tips around it.

Sensor design and principle

Sensor fabrication is described in Fig. 2. The plasmonic nose is made up of seven "olfactory receptors", each containing a single nanoparticle morphology: i GNB, ii GNSph, iii GNR_{670}, iv GNR_{730}, v $GNSht_{680}$, vi $GNSht_{700}$, vii GNStr (Fig. 2a). Each nanoparticle morphology was mixed with Tollens' reagent ($[Ag(NH_3)_2]OH$) and then embedded in an agarose matrix and placed separately in an optical plastic cap of 200 µL microtube strips with

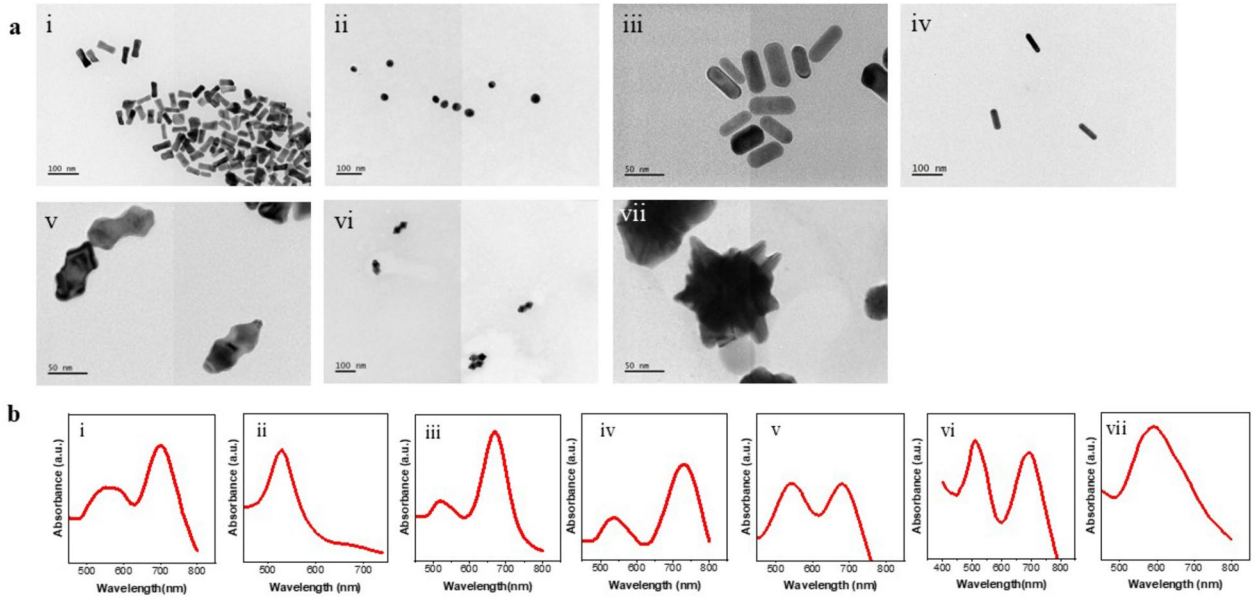

Fig. 1 Characterization of gold nanoparticles used in sensor fabrication**. a** TEM micrographs showing the different morphologies of AuNPs used in plasmonic nose fabrication. i gold nanobones GNB, ii gold nanospheres GNSph, iii gold nanorods longitudinal plasmon of 670 nm GNR_{670}, iv gold nanorods longitudinal plasmon of 730 nm GNR_{730}, v gold nanoshuttles longitudinal plasmon of 680 nm $GNSht_{680}$, vi gold nanoshuttles longitudinal plasmon of 700 nm $GNSht_{700}$, and vii gold nanostars GNStr. **b** Localized surface plasmon resonance (LSPR) spectrum of the seven AuNPs morphologies used in sensor fabrication

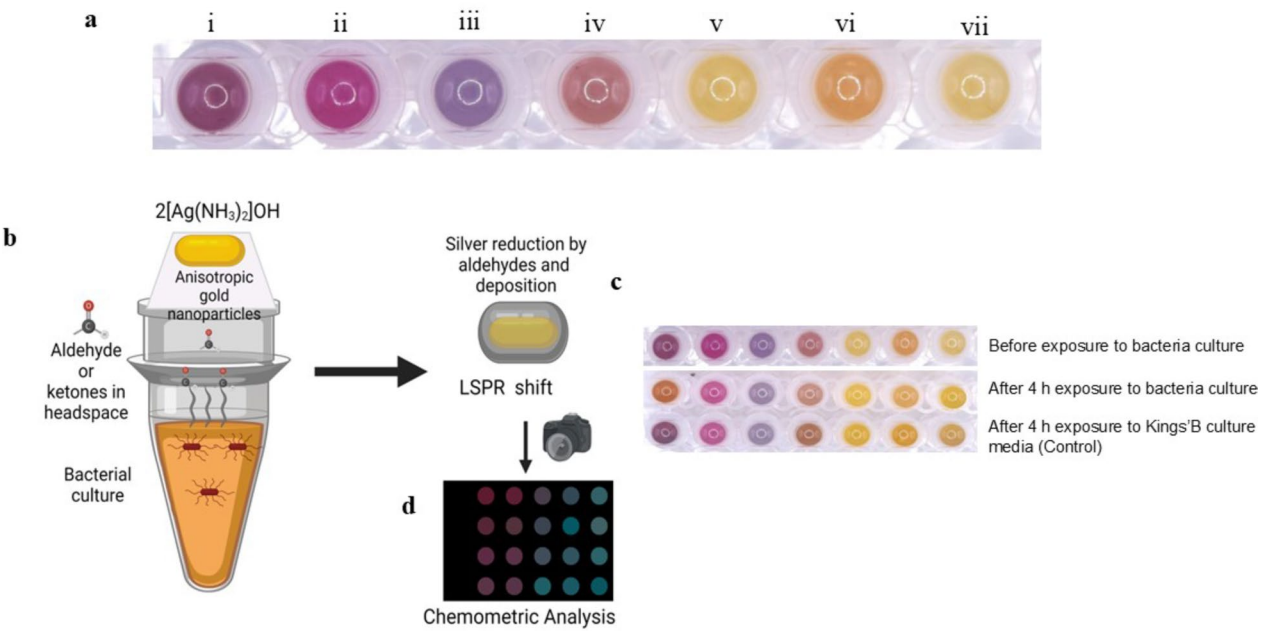

Fig. 2 Schematic representation of the plasmonic nose sensor design. **a** Sensor strip containing seven "olfactory receptors" with distinct nanoparticle morphology: i GNB, ii GNSph, iii GNR_{670}, iv GNR_{730}, v $GNSht_{680}$, vi $GNSht_{700}$, and vii GNStr. Each nanoparticle morphology is embedded in agarose and mixed with Tollens' reagent, $2[Ag(NH_3)_2]OH$. **b** During the detection test, a suspension of bacteria in King´s B culture media is loaded in the microtube, and then the sensor cap is placed in the tube. **c** During bacteria metabolism, if some volatile aldehydes and ketones are released to the headspace of the tube, these molecules will reduce the Tollens' reagent, and metallic Ag will be deposited on the AuNP of the sensor, inducing a plasmon change that can be visualized in a color change of the sensor. **d** The color changes are analyzed with a MatLab algorithm designed in this work to obtain the ΔRGB for further chemometric analysis

seven positions. To perform the detection test, 60 µL of bacterial suspension with $OD_{600}=0.1$ are dispensed in the tubes of the sensor strip. Then, the sensor cap strip containing the seven AuNP morphologies was placed in the tube strip. If the tested bacteria produce volatile aldehydes during their metabolism, the aldehydes released to the headspace of the tube will reduce the Tollens' reagent, conducing to the silver reduction from Ag^{+1} to Ag^{0}. Thus, the metallic silver will be deposited around the nanoparticles (Fig. 2b) with a modification of the original plasmon of each AuNPs, resulting in a visible color change of the olfactory receptor with respect to the color before exposure to bacteria (Fig. 2c). It is expected that each bacteria produce different type or different concentration of aldehydes that allows a clear optical differentiation of each tested bacteria. In parallel to the test, as a control assay, a sensor strip containing only non-inoculated culture media is added to subtract the effect of culture media VOCs. After the incubation time, a picture of the sensor is captured with a digital camera, and the image is processed in a Matlab algorithm presented further ahead (Fig. 2d). The RGB values of each olfactory receptor in the control strip are subtracted from the resulting RGB value of the tested bacteria sensor strip, and the differential RGB (ΔRGB) is then used for chemometric analysis.

Image analysis algorithm

Example results from the sample identification and RGB color extraction are shown in Fig. 3, also illustrating the different steps in the process. The example image (1824×1537 pixels) contains 42 samples of different colors, arranged in a grid of 6×7 samples. The average grey levels along the horizontal and vertical axes of the example image are shown in Fig. 3a, using a window size for the moving mean of 70 pixels. The resulting local maxima are indicated by the red markers in Fig. 3a and

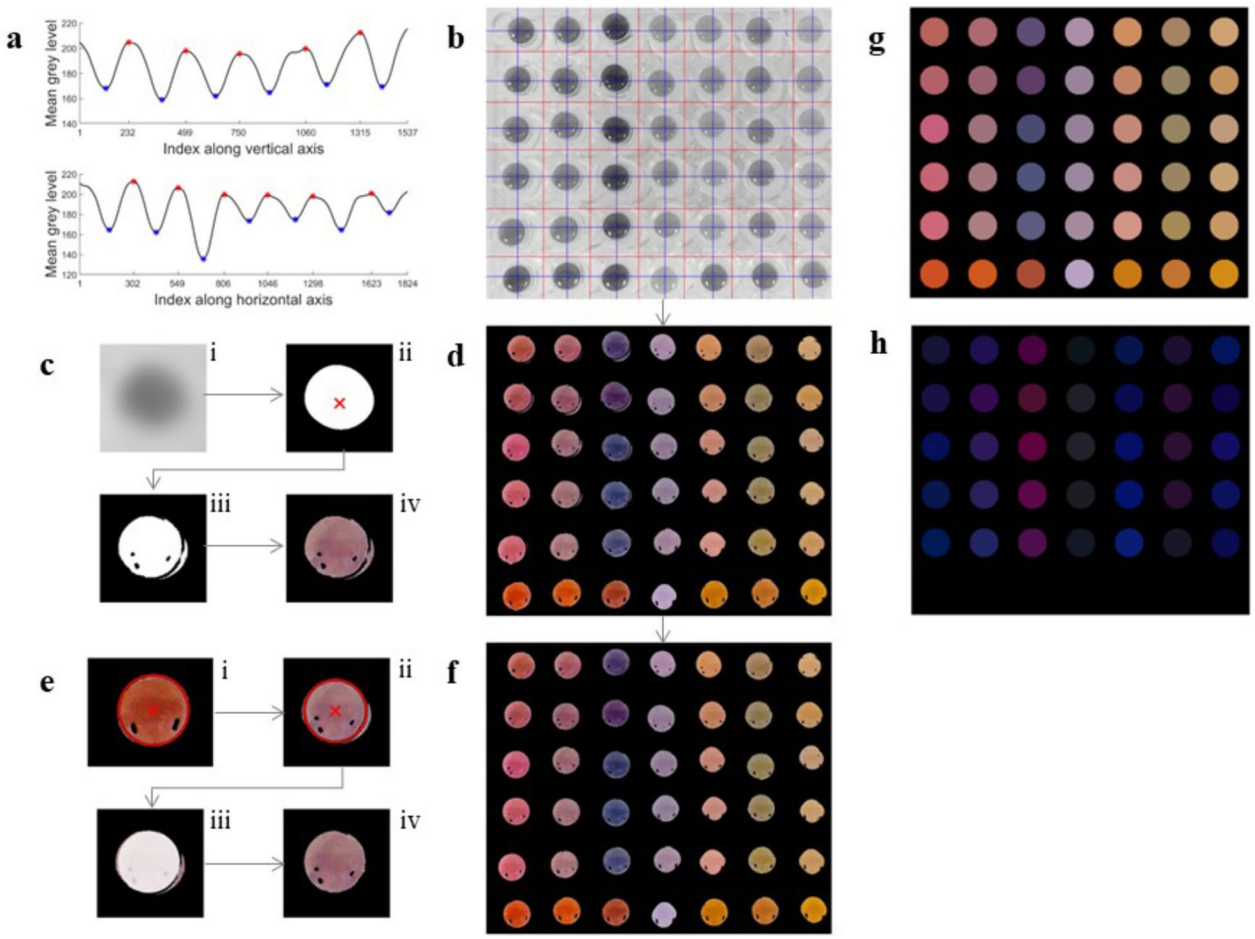

Fig. 3 The image analysis process for sample identification and color extraction applied to an example image. The subfigures on the left show the different main steps involved. **a** sample grid and midpoint identification, **c** sample extraction, and **e** sample image trimming. The subfigures **b**, **d**, and **f** show the results of each of these three main steps. **g** examples of extracted RGB color intensities. **h** the RGB intensity differences (ΔRGB) when using the bottom sample of each column as the reference for the rest of the column samples

the resulting grid is shown in Fig. 3b. The resulting local minima are indicated by blue markers and lines in Fig. 3a, b, respectively.

Figure 3c shows the process of sample extraction in four steps for one of the individual sample images (row 3, column 2 in the sample grid): (i) the Gaussian-filtered greyscale image, using a standard deviation of 20 pixels, (ii) the binary mask of the filtered image, using a threshold factor of 0.95, and the location of the midpoint indicated by a red marker, (iii) the final binary mask after intersection between the binary masks for the filtered and unfiltered images, and (iv) the extracted sample. Figure 3d shows the whole image after the same procedure has been applied to each individual sample image. As can be seen, the binary mask effectively removes the non-sample parts of the image as well as the light reflections in the sample. Figure 3e shows the steps involved for the example image: (i) identification of the most circular sample (row 6, column 3 in the grid), with the centroid and the circle given by the equivalent diameter indicated in red, (ii) the same circle placed at the centroid of the sample from Fig. 3c, (iii) the circular mask superimposed in white on the sample, and (iv) the trimmed sample. Figure 3f, finally, shows the whole image after this procedure has been applied to all samples. After the extraction of the samples in Fig. 3f, the average RGB color values of each sample are obtained (Fig. 3g), and then the differences in RGB color intensity between the sample and culture media (control) located in the bottom row are calculated (ΔRGB). Figure 3h shows the resulting RGB colors and the RGB color differences for the example image.

Chemical response and classification of plant pathogenic bacteria

The plasmonic nose sensor could reliably discriminate the tested bacteria after two hours of incubation and onwards, according to an HCA analysis; however, before this time there was a notorious misclassification (Additional file 1: Figure S1). Figure 4a shows the plasmonic response of the nose sensor after incubation with five different phytopathogenic bacteria for 3 h. It is notorious that King's B culture media also produced volatile compounds modifying the original particle plasmon, which is why the RGB values of this control experiment were subtracted from tested samples. In a visual evaluation, the most prominent differences are given by the most anisotropic nanoparticles like gold nano bones, gold nanorods with longitudinal LSRP of 730 nm, gold nanoshuttles of both sizes, and gold nanostars. The anisotropic

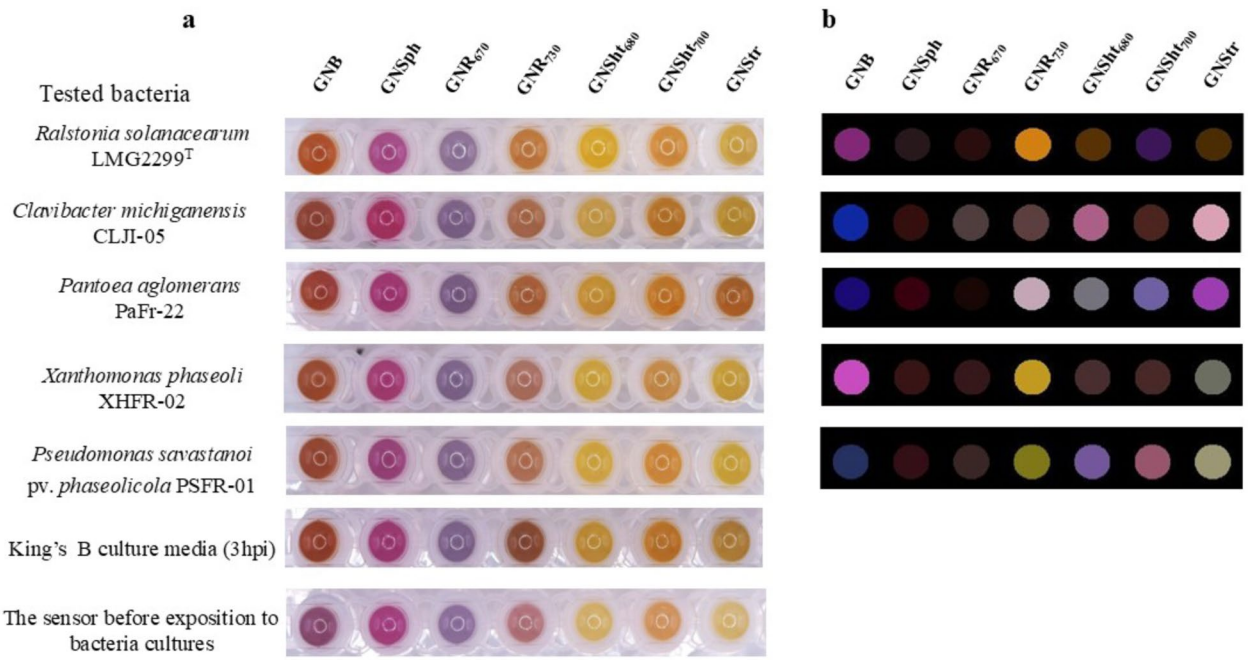

Fig. 4 Visualization of plasmon shift and ΔRGB pattern of the sensor after incubation with five different phytopathogenic bacteria. **a** Optical image of sensor strips after incubation with five different phytobacteria for 3 h. A sensor strip containing King's B liquid culture media was included as a control. the RGB value of each "receptor" in the control strip is subtracted from its homologous "receptor" in the test strip (incubated with bacteria), and this differential RGB value is called ΔRGB. **b** ΔRGB pattern of the five tested phytobacteria obtained with the plasmonic nose after 3 h of incubation. The nanoparticle shape in the "olfactory receptor" is indicated at the top. hpi: hours post incubation

nanoparticles have been reported to present a higher refraction index, enabling them to be more sensitive to the chemical environment and increasing the detection in sensor systems compared with isotropic particles such as spheres. Figure 4b shows the ΔRGB fingerprint of the sensor after 3 h of incubation (using images from Fig. 4a). A clear difference is observed for each bacterium, enabling this sensor to classify bacteria species.

To clarify the optical differences, some classification methods were applied using the numerical values of ΔRGB. Firstly, an HCA was performed on the five tested bacteria at 3 and 4 h post incubation (hpi) (Fig. 5a, b). It is also noticeable that HCA analysis shows a similar clustering of data at 3 and 4 hpi, and at this point, we consider that a reliable discrimination can be reached after 2 h of incubation (Additional file 1: Figure S1). At both tested times two main categories were obtained; in the first group *Ralstonia solanacearum* LMG2299^T and *Xanthomonas phaseoli* XHFR-02 were grouped at 3 h, but after 4 hpi, *Pantonea aglomerans* PaFr-22 was subsequently added to this group, and the second group stands the presence of *Pseudomonas savastanoi* pv. *phaseolicola* PSFR-01 and *Clavibacter michiganensis* CLJI-05. This may be explained by common volatile aldehydes and alpha-hydroxy ketones produced by both strains. The LDA classification method was also applied, showing that the sensor allows a clear separation of bacteria species groups (Fig. 5c, d). With both discrimination methods, we can conclude that the plasmonic-nose sensor can easily differentiate between bacteria species.

Plasmonic nose performance

To validate the performance of the designed sensor, Koch's postulates were applied using *P. savastanoi* pv. *phaseolicola* PSFR-01 (Pp) in "Cacahuate" bean plants. The bean plants were infected with the Pp strain, and once the leaves showed symptoms of halo blight (necrotic spots surrounded by halo chlorosis, see Fig. 6a), the bacterium was reisolated and named Ppb, showing a similar colony morphology to Pp in King's B agar. Also, a *Pseudomonas* sp. isolated from leaf blight in "Cacahuate" bean crop in field (Fig. 6d) was tested in the sensor (Plb). The reference strain (Ppb) and the field isolate (Plb) showed a hypersensitive response (HR) in tobacco leaves (Fig. 6b, c). The three tested bacteria showed fluorescent pigment under UV light typical of *Pseudomonas* (Fig. 6e). The three strains were then incubated in the sensor under the same conditions described above and the optical behavior of LSPR in the sensor was monitored for 4 h to proceed with the optoelectronic analysis. As is shown in

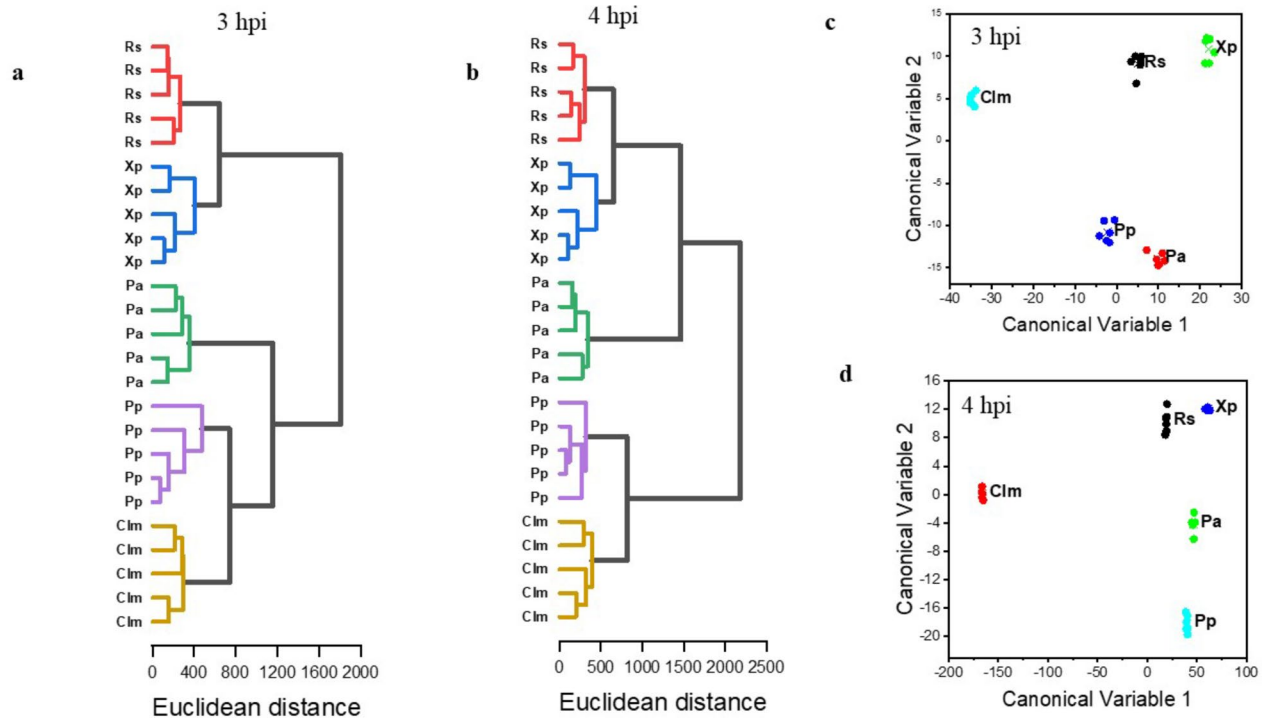

Fig. 5 Chemometric analysis of bacteria species classification. **a**, **b** Hierarchical cluster analysis (HCA) for differentiating five plant pathogenic bacteria species at 3 and 4 hpi. **c**, **d** Linear discrimination analysis (LDA) at 3 and 4 hpi. Experiments were performed in five replicates. Rs: *Ralstonia solanacearum* LMG2299.^{T}, Xp: *Xanthomonas phaseoli* XHFR-02, Pa: *Pantoea aglomerans* PaFr-22, Pp: *Pseudomonas savastanoi* pv. *phaseolicola* PSFR-01, Clm: *Clavibacter michiganensis* CLJI-05

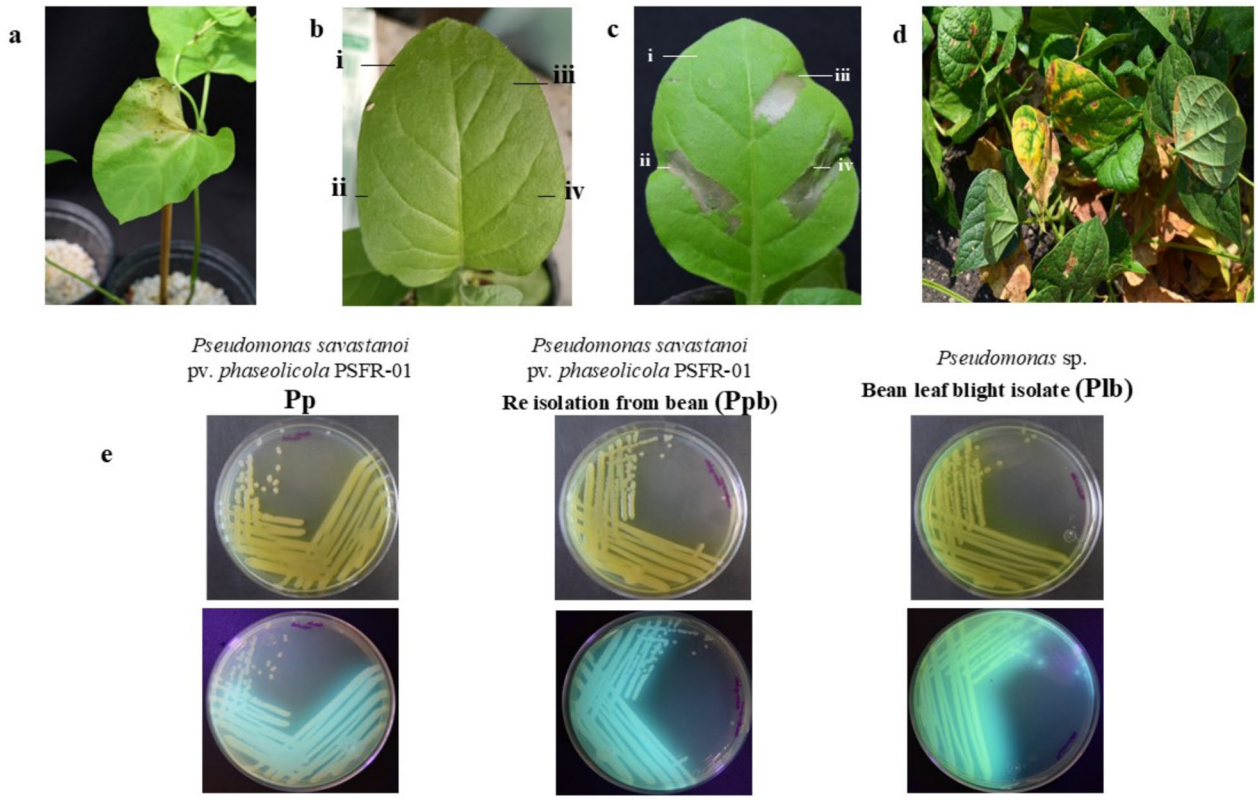

Fig. 6 Infection model for sensor performance. **a** Halo blight symptoms in infected "cacahuate" bean plants with *Pseudomonas savastanoi* pv. *phaseolicola* PSFR-01 (Pp) under greenhouse conditions. **b**, **c** HR response in tobacco leaves before and after infiltration with i sterile solution of 10 mM $MgCl_2$, ii *Pseudomonas* sp. isolated from leaf blight in bean plants in the field (Plb), iii *P. savastanoi* pv. *phaseolicola* PSFR-01 re-isolated from experimentally infected bean (Ppb), and iv *P. savastanoi* pv. *phaseolicola* PSFR-01 reference strain. **d** Bean plant showing symptoms of leaf blight, the isolated *Pseudomonas* sp. was used for testing the sensor. **e** Colony morphology of three tested *Pseudomonas*, lower pictures were taken under UV light to show fluorescence

Fig. 7a, at 1 h post incubation (hpi), the sensor classified Pp and Ppb in two closely related clusters and Plb showed a bigger Euclidean distance to the other two groups, no misclassification was observed using HCA methods at 1 hpi. However, at 3 hpi both Pp and Ppb are classified in the same cluster without misclassification of Pp and Ppb in the cluster of Plb (Fig. 7b). One of the five sensor replicates of Plb was misclassified in the group of Pp and Ppb (highlighted in green box). Using the HCA classification model at 3 hpi, we can observe a sensor accuracy of 93%. The LDA analysis (Fig. 7c, d) show that Pp and Ppb are closely related by both canonical variables 1 and 2, at 1 and 3 hpi, being that the canonical variable 2 allows the best classification of Ppb in the Pp group. Meanwhile, Plb shows a significant separation in both canonical variables from the groups of Pp and Ppb, confirming the power of this plasmonic nose sensor to perform an accurate identification and classification of plant pathogenic bacteria, reaching an accuracy of 100% using LDA classification model.

Discrimination between *P. savastanoi* pv. *phaseolicola* PSFR-01 and saprophytic fluorescent and non-fluorescent bacteria isolated from bean leaves

We observed the colony morphology of the reference strain *P. savastanoi* pv. *phaseolicola* PSFR-01 and two fluorescent and one non-fluorescent bacteria strains isolated from bean leaves (Additional file 1: Figure S2). The isolates Col2, Col3, and the reference strain show different fluorescence under UV light, but Col1 does not fluoresce; however, Col2 shows different colony morphology compared to the reference strain and other isolates. We performed an incubation of those fluorescent bacteria in the plasmonic-nose sensor in an incubation period of 4 h. The HCA of the three fluorescent bacteria and the reference strain showed that the dendrogram is divided into two main groups, the first group including *P. savastanoi* pv. *phaseolicola* PSFR-01 and Col3, and a second group including Col1 and Col2 (Additional file 1: Figure S3a). In the LDA test, the 2-D canonical plot shows clear discrimination between isolated fluorescent colonies compared to reference strains (Additional file 1: Figure S3b).

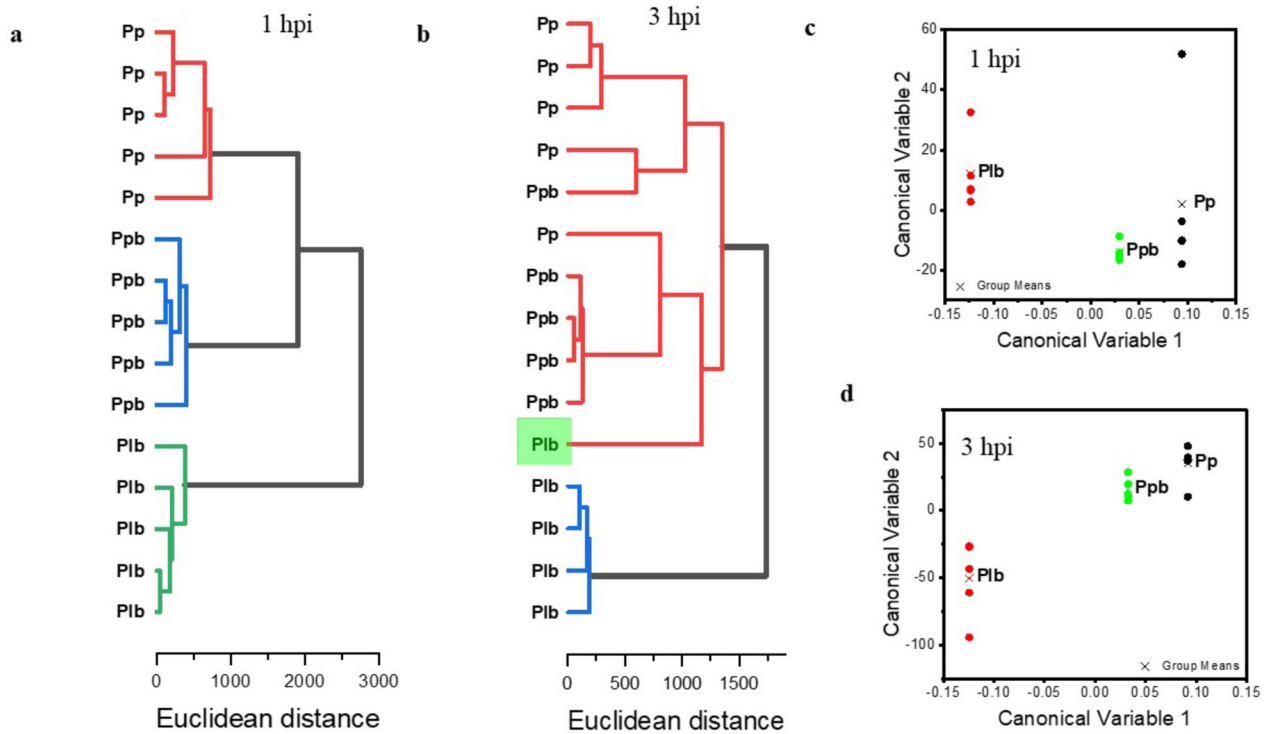

Fig. 7 Chemometric analysis for sensor validation. **a**, **b** HCA for classification of the three preparations of *Pseudomonas*. Pp: *P. savastanoi* pv. *phaseolicola* PSFR-01; Ppb: *P. savastanoi* pv. *phaseolicola* PSFR-01 re-isolated from the experimental model; Plb: *Pseudomonas* sp. tested at 1 and 3 hpi. **c**, **d** LDA analysis at 1 and 3 hpi

No misclassification was observed for either method, confirming that the plasmonic-nose sensor described here shows a strong discrimination ability for saprophytic fluorescent and non-fluorescent bacterial isolates from symptomatic bean leaves.

Discussion

During bacteria metabolism, certain organic volatile compounds (VOCs) are produced and released to the headspace, some of which belong to aldehydes and ketones. VOCs have previously been used for bacterial identification and classification using advanced instrumental techniques like gas chromatography (GS) and mass-spectrometry (MS), which offer reliable results and high sensitivity in detection and quantification. However, the access to this kind of instrumentation is not widespread enough for application in a routine diagnosis. New methods based on optical sensors could help to reduce costs for diagnostics and provide accessibility to quick and reliable bacteria identification based on VOCs.

In this study, we have proposed such a sensor, using the properties of gold nanoparticles. Localized surface plasmon resonance (LSPR) and the high refractive index that results from the morphology of the gold nanoparticles allow the design and fabrication of a nanostructured optical sensor for the detection of different analytes by modifying the LSPR and coupling this detection to basic spectroscopic techniques such as UV–Vis and optoelectronic analysis. According to the principle of our plasmonic-nose sensor, aldehydes and alpha-hydroxy ketones can reduce the Tollens' reagent presented in the reactive matrix of the sensor and produce metallic silver (Ag^0) that will be deposited around the nanoparticle, consequently modifying the original LSPR of the sensor AuNP. When applying the sensor to different plant pathogenic bacteria, the behavior in LSPR differed depending on the type of aldehydes or alpha-hydroxy ketones produced by the tested bacteria and their redox potential and concentration. Hence, an evident optical differentiation of the bacteria species tested here was observed.

This agrees with previous findings. For example, it has been reported that acetoin (classified as alpha-hydroxy ketone) is produced by *Clavibacter michiganensis* and *Pantoea aglomerans* (Davis et al. 1984; Guevarra et al. 2021) whereas *Xanthomonas* is not able to produce this volatile (Soudi et al. 2011). Acetoin is produced during the primary metabolism of bacteria derived from the glycolytic pathway, specifically derived from pyruvate. In our observations, in Fig. 5a, the bacteria genera *Clavibacter* and *Pantoea* are clustered together in the first 3 h

of incubation, but *Xanthomonas* is clustered separately from these bacteria species in both discrimination methods. It is important to highlight that bacteria were tested in King's B media, which contains glycerol as a carbon source and as an intermediate product of this primary metabolism that will produce pyruvate. On the other hand, according to the bacterial growth rate, the volatile metabolites will be produced and released in different concentrations in the tube headspace, modifying the reduction reaction rate in the sensor and helping to differentiate between bacteria species.

The detection of formaldehyde using plasmonic sensor arrays in liquid reaction media based on reduction of Tollens' reagent has been reported previously. Duan et al. (2019) observed a blue shift in LSPR sensor nanoparticles (gold nanobones) depending on the formaldehyde concentration added to the sample. The TEM analysis and EDX elemental maps show that a layer of metallic silver is deposited around the sensor nanobones after aldehyde oxidation with Tollens' reagent. In a similar work, Wang et al. (2021) reported the use of gold nanorods for the quantification of volatile formaldehyde in indoor environments. Likewise, they observed that after the reduction of Tollens' reagent by the formaldehyde, the silver is deposited around the gold nanorods, and the degree of silver deposition increases when the formaldehyde concentration grows, forming a core–shell Au@Ag nanoparticle.

Li et al. (2020) reported the feasibility of a plasmonic sensor in discriminating aldehydes in a liquid environment. The sensor was fabricated with spherical gold nanoparticles of different sizes (40, 22, and 13 nm) in combination with Tollens' reagent, and the LSPR shift was evidenced also as a colorimetric change in the sensor was observed before and after the redox reaction between an aldehyde and Tollens' reagent. This colorimetric change was then analyzed using the ΔRGB data of each image, which was used for further chemometric analysis. It is important to note that the classification of aldehydes is based on their redox potential and chemical structure. Short-chain aldehydes show a rapid reactivity with Tollens' reagent. Meanwhile, long carbon chain aldehydes like heptaldehyde have an oxidation rate that is slower compared with formaldehyde, acetaldehyde, and butyraldehyde, allowing clear chemical discrimination using the ΔRGB fingerprint.

In the optoelectronic analysis of color change response, similar approaches have been proposed previously but, as it seems, with less automated image analysis and for more regular and less noisy sample images. Zhang et al. (2014) calculated color difference maps for samples based on scanned colorimetric sensor arrays. However, it is not clear whether they used any particular image analysis method for automatically identifying and extracting the sample color values. Salles et al. (2014) developed an iPhone app for determining RGB values of colorimetric spot-tests on paper, which was used by Bueno et al. (2015) to extract RGB values from photos of arrays of membranes with pH indicators. The exact functionality of the app is not provided, and it is not clear how much manual interaction was required by the user. An approach similar to our procedure for sample identification was proposed by Bordbar et al. (2020a, b) for samples on paper; however, their method requires manual identification and extraction of each sample spot through a graphical user interface. In our method, the samples are automatically identified by the image analysis algorithm after a few general parameters are set. In the method of Bordbar et al (2020a, b), the average color values are calculated based on the whole manually extracted sample shape, which is appropriate for scanned sample spots on paper; our method, however, is able to handle the noisier photographs of plastic tube racks, as the algorithm automatically removes parts of the sample shapes that contain light reflection in the test tubes.

Additionally, in comparison with the work reported by Bordbar et al. (2020a, b) the plasmonic-nose sensor presented here allows real-time monitoring without the need to remove the sensor substrate for data acquisition, as our sensor allows to take a direct photograph of the sensor substrate without disturbing the reaction process. In the chemometric analysis we showed a clear classification of five plant pathogenic bacteria species using two classification methods, and a more accurate classification was obtained after 3 h of incubation. This sensor can accelerate the correct identification of plant pathogenic bacteria in field samples coupled with traditional microbiological methods. As shown in Figs. 6 and 7, the sensor exhibited a high accuracy rate above 90% for correct classification of the *P. savastanoi* pv. *phaseolicola* re-isolated from leaves in an infection model of halo blight disease. In a previous report, Bordbar et al. (2020a, b) designed a nanostructured chemical nose sensor fabricated for the detection of clinical infectious bacteria with an accuracy of 100% using HCA and PCA classification methods; in our work, HCA method presented a 93% of accuracy and using LDA it reached 100%. It is clear that our plasmonic sensor can differentiate between *P. savastanoi* pv. *phaseolicola* and other fluorescent and saprophytic bacteria found in bean leaves presenting leaf blight symptoms (Additional file 1: Figures. S2 and S3). The application of this sensor allows for quick and reliable diagnosis, reducing cost and time compared with the traditional molecular diagnostic of bacteria diseases. This is the first report showing the application of plasmonic nose chemosensor

for detection of plant pathogenic bacteria coupled with optoelectronic analysis.

Conclusion

In this study, we report a plasmonic nose chemosensor based on seven AuNPs morphologies and couple it to an image analysis algorithm for RGB extraction designed in our research group, with a view to plant health innovation. The plasmonic sensor can be used for real-time discrimination between bacteria species using a chemical reaction coupled with photo-image analysis. The plasmonic sensor enables reliable discrimination of five phytopathogenic bacteria after 3 h of incubation at 30 °C, shows high accuracy classification of *P. savastanoi* pv. *phaselicola* isolated from a halo blight infection model in bean, and can discriminate from fluorescent and saprophytic bacteria isolated in the field samples from the reference strain *P. savastanoi* pv. *phaseolicola* PSFR-01. Thus, this study provides a new approach to an effective, reliable, and rapid test that is useful for detecting pathogenic microorganisms isolated from plant materials.

Methods

Chemicals and glassware treatment

Gold (III) chloride trihydrate ($HAuCl_4$, 99%), sodium borohydride ($NaBH_4$, ≥ 99%), hexadecyl trimethylammonium bromide (CTAB) ($C_{19}H_{42}BrN$, ≥ 99%), l-ascorbic acid ($C_6H_8O_6$, 99%), silver nitrate ($AgNO_3$, ≥ 99%), and agarose (Molecular biology grade) were purchased from Merck/Sigma-Aldrich (US). Tollens' reagent (diamine-silver hydroxide) $[Ag(NH_3)_2]OH$ was freshly prepared by a combination of 500 µL of $AgNO_3$ (0.5 M), 520 µL of NH_4OH (25%), 325 µL of NaOH (3 M) and then take the mix to 10 mL with deionized water. All glassware for gold nanoparticle synthesis and storage was washed with a basic mixture using the standard clean method no. 1 of RCA company (TL1, RCA SC-1), H_2O:H_2O_2 30%: NH_4OH 25% (5:1:1) and heated to 80˚C for 10 min, then rinsed with ultrapure water ten times and dried.

Gold nanoparticle (AuNP) synthesis

Seeds nanoparticles Briefly, a seed nanoparticle solution was formed by mixing equal volumes of $HAuCl_4$ (0.5 mM) and CTAB (200 mM). After that, the solution was stirred for one minute, whereupon a suitable amount of freshly prepared ice-cold $NaBH_4$ was added to a final concentration of 0.6 mM, which was then stirred for one minute more. Finally, the solution was kept for two hours at room temperature without disturbance.

Gold nanospheres (GNSph) In 5 mL of CTAB solution (0.2 M), 200 µL of $HAuCl_4$ (25 mM), and 75 µL of ascorbic acid (80 mM) were added. Then, the pH was adjusted to pH 11 with NaOH (1 M); after that, 15 µL of seed nanoparticles were added to the growth solution and incubated at 37 °C for 18 h (Cheng et al. 2011).

Gold nanobones (GNB) Growth solution was prepared in 25 mL of CTAB (0.2 M) containing 1 mL of $HAuCl_4$ (25 mM), then pH was adjusted to 7.0 using NaOH (1 M); after that, 600 µL of $AgNO_3$ (16 mM), 500 µL of ascorbic acid (80 mM), and 60 µL of seeds nanoparticles were added. The reaction mix was incubated at 37 °C for 18 h (Cheng et al. 2011).

Gold nanorods (GNR 670 and 730 nm) Gold nanorods were synthesized according to Wang et al. (2015). In brief, using a growth solution of 25 mL of CTAB (0.2 M) containing 1 mL of $HAuCl_4$ (25 mM), the pH was adjusted to 4.5 for the synthesis of 670 nm longitudinal LSPR rods, and for 730 nm LSRP rods, the pH was adjusted to 2.5, after that, 450 µL of $AgNO_3$ (16 mM) and 375 µL of ascorbic acid (80 mM) were added to growth solution, then 60 µL of seeds nanoparticle solution was added and hand mixed for 30 s then incubated for 18 h at 28 °C.

Gold nanoshuttles (GNSht 680 and 700 nm) Gold nanorods with longitudinal LSPR of 670 and 630 nm were used as seeds for nanoshuttles synthesis. Briefly, nanoshuttles were synthesized according to Bai et al. (2014), 10 mL of rods seed particles suspended in CTAB (0.1 M) were added in 10 mL of glycine (0.2 M), then pH was adjusted to 8.5 using NaOH (2 N), then 80 µL of $HAuCl_4$ (25 mM) and 400 µL of $AgNO_3$ (10 mM) were added. The mix was incubated for 5 min at 25 °C in a water bath, and 400 µL of ascorbic acid (100 mM) was immediately added and mixed for 30 s by shaking inside the water bath. The reaction mix was incubated for one hour at 25 °C in the water bath.

Gold nanostars (GNStr) Nanostars were synthesized according to the previous report (Sau et al. 2011). In 10 mL of CTAB (0.2 M), 320 µL of $HAuCl_4$ (25 mM) was added; then, 120 µL of ascorbic acid (100 mM) and 376 µL of $AgNO_3$ (16 mM) were added, and the volume was adjusted to 20 mL using deionized water. The growth solution was mixed for one minute and then incubated for 18 h at 28 °C.

Characterization of gold nanoparticles

The solutions of gold nanoparticles were characterized by recording a visible spectrum from 400 to 850 nm in a

spectrophotometer to acquire the LSPR curve. For transmission electron microscopy (TEM) visualization, the gold nanoparticles were washed three times by centrifugation (8160 *g*, 10 min) and resuspended in deionized water. The nanoparticle solution was diluted properly, and then an aliquot was deposited on a copper grid; the micrographs were acquired in a JEOL TEM JEM2010 FEG.

Plasmonic nose sensor fabrication and set-up

The plasmonic-nose sensor is designed to contain seven "olfactory receptors" corresponding to the seven AuNPs morphologies described previously and illustrated in Fig. 1. The sensor prototype was fabricated using a 200 µL microtube strip (8 tubes per strip) with domed transparent caps (Axygen). The cap of the tubes was the base for the plasmonic sensor, and the tube contained the tested bacteria (Fig. 2). The sensor matrix was formed by a mix of ultrapure agarose 0.5% mixed with Tollens' reagent in a final concentration of 87.5 µM, then 32 µL of this solution was mixed with 28 µL of gold nanoparticles (without any dilution after synthesis, with only an extra step of washing twice and resuspended in deionized water). This mix was placed in the inside part of the domed cap of the tube and was allowed to gel at room temperature (a cap in the strip for each AuNP morphology, Fig. 2). The optimal concentration of agarose, Tollen's reagent, and gold nanoparticles in the mix was standardized previously. Tube and cap stripes were previously sterilized at 121 °C, 15 pounds/inches^2 for 15 min. Sensor fabrication was prepared under sterile conditions in a laminar flow hood.

Sensor operation

The sensor tubes were filled with 60 µL of tested bacteria suspension or uninoculated culture media. Once the cap lid containing the sensor was closed, the sensor strips were incubated at 30 °C with a strip containing only culture media and a sensor strip without culture media or bacteria. Then, the sensor was removed from the incubator chamber, and a photograph of the sensor was taken under "cold" white LED light. The working distance between the camera and sensor strips was 45 cm, and photographs were taken using a Nikon DX-VR camera. The photographs were used for the RGB extraction process using our designed algorithm described above.

The following plant pathogenic bacteria were used to test the sensor: *Ralstonia solanacearum* LMG2299^T, *Clavibacter michiganensis* CLJI-05, *Pantoea aglomerans* PaFr-22, *Xanthomonas phaseoli* XHFR-02, and *Pseudomonas savastanoi* pv *phaseolicola* PSFR-01. The bacteria species belong to the Plant Pathology Lab of Chávez-Ramírez B and were isolated from field samples and characterized by molecular techniques. Bacteria were grown in solid King´s B culture media and incubated at 28 °C for 3–5 days. For sensor experiments, a bacteria suspension was prepared in liquid King´s B culture media and then adjusted to an optical density of 0.1 at 600 nm, then 60 µL of bacteria suspension was dispensed in the tube strips, and the sensor strip cap was placed and closed carefully avoiding the bacteria suspension splash in the sensor nose.

Validation of sensor performance

To validate the power of the plasmonic nose sensor for the accurate detection and classification of plant pathogenic bacteria, an infection model of halo blight disease was carried out with the reference strain *Pseudomonas savastanoi* pv. *phaseolicola* PSFR-01 (Pp). First, a bacteria suspension of Pp (1×10^9 CFU/ mL) was aspersed on the leaves of two-week-old "Cacahuate" bean plants until runoff. The plants were incubated in a greenhouse with a 100% moisture environment condition until symptoms of halo blight were showing. A sample of symptomatic leaves was collected and rinsed with tap water, then sanitized with sodium hypochlorite 1% for 3 min, rinsed with sterile distilled water, and then ground in a sterile mortar; an aliquot was streaked in King's B solid culture media, and the fluorescent colonies were re-cultured in a King's B culture media for purification, the reisolated bacterium was named (Ppb).

The reference strain Pp, reisolated Ppb, and a *Pseudomonas* sp. (Plb) isolated from leaf blight lesions in a crop of "Cacahuate" bean, were infiltrated in tobacco leaves to show the HR response. Finally, the three different preparations of *Pseudomonas* (Pp, Ppb, and Plb) were incubated in the nose sensor in the conditions described above and were monitored for 3 h.

For experiments of discrimination of fluorescent bacteria, three fluorescent and saprophytic bacterial strains, Col1, Col2, and Col3, were isolated from bean leaves. To test if the sensor can differentiate the fluorescent and saprophytic bacteria from the reference plant pathogenic strain *P. savastanoi* pv. *phaseolicola* PSFR-01, the sensor was incubated with the three colonies and the reference bacteria under the conditions described above.

Optoelectronic algorithm for image analysis and RGB extraction

RGB extraction was performed on the photographs using the following algorithm implemented in Matlab. Each step in the algorithm is shown for an example image in Fig. 3. In the first step of the algorithm, a grid of vertical and horizontal lines is identified in the image and divided into smaller images, which are further processed. Grid lines between rows and columns of samples are identified by first converting the image to greyscale and then

calculating the average grey levels of pixels (a value from 0 to 255) of each row and column. As the colored samples generally have a lower value (i.e., are darker) than the area between the samples, the grid lines are drawn where the highest average row and column values are found. The moving mean of the grey level is calculated before maxima are identified to remove noise. The window length (number of pixels) for the moving mean is a parameter that has to be set depending on the image resolution and individual sample size. All local maxima are identified using the Matlab function islocalmax. To avoid identifying several local maxima and drawing more than one grid line between samples due to slight variations in the grey levels even after taking the moving mean, the prominence of each maximum is determined, and only the maxima with a prominence above a pre-defined threshold are kept. The prominence is defined as the difference between the local maximum and whichever minimum between the peak and the nearest higher peak to the left or right is the highest. For the example image, a prominence threshold of 1 on the grey level scale is sufficient to remove extra lines between samples. To identify the midpoints of the samples, a corresponding procedure is carried out, but for local minima instead, using the Matlab function islocalmin. The next step is to cut out the parts of each sample image that belong to the colored sample itself and remove the rest, including light reflections in the sample. For this purpose, a binary mask is created from the greyscale image, where all pixels with a grey level below a certain threshold (i.e., darker, belonging to the sample) are set to 1, and all pixels above the threshold are set to 0. The threshold is, by default, taken as the mean grey level over the sample image but is multiplied by a factor that can be set to slightly below or above 1 for fine-tuning the mask. The reason for performing this step individually for each sample is that the binary mask threshold is adapted to the average grey level of each sample image, which gives better results than applying the same threshold to the whole image.

In case the difference in grey levels between the sample and its vicinity is not very high, the mask risks becoming noisy and may contain parts that belong to the actual sample and parts that do not. For this reason, a Gaussian filter is first applied for noise reduction. The Matlab function imgaussfilt is used, for which the filter's standard deviation (number of pixels) has to be chosen depending on the sample size in pixels. The sample part of the binary mask is then identified as the 4-connected component (identified using bwlabel) containing the midpoint of the sample identified in the previous step. The intersection between the sample part of the noise-reduced binary mask and the binary mask of the unfiltered image gives the final binary mask for sample identification. After this step, some of the extracted samples may still contain parts that do not belong to the sample, which may be due to shadow effects, samples not photographed perfectly from above, or a low difference in grey value between the sample and its surroundings. Therefore, as a final step, the extracted samples are trimmed by creating a circular binary mask from the most well-identified sample and applying this to the rest of the samples. The circularity (equal to 1 for a perfect circle and below 1 for non-circular shapes) of each binary mask is determined using the Matlab function regionprops, and the sample with the highest circularity is chosen. The equivalent diameter of this sample shape, given by regionprops, is then taken as the diameter of the circular mask. The centroid of each sample binary mask from the previous step is determined by applying regionprops to each sample, and the circular binary mask is placed with its center at each sample centroid. Only the parts of the sample within the circular binary mask are kept.

Additional steps need to be taken in case there are no samples in all grid positions. The reason is that even if there is no sample, there will still be an image that is processed as above, and as there is no a priori information on whether cells contain samples or not, non-sample shapes may be identified and extracted as samples. However, these are usually small and/or non-circular. Therefore, a size threshold is defined to avoid small but circular shapes being chosen as the representative sample for the circular mask above, and a threshold value is defined for the relative difference between the circular mask and the shapes to which it is applied. Shapes that are too different from the representative sample are removed. In the example image, these thresholds were not critical, as there is a full grid of samples, but for other images with similar sample sizes in pixels, a suitable size threshold was found to be 20 pixels, and a suitable difference threshold was 0.5. The Additional file 2: Table S1 lists the parameters that need to be set as well as their values for the example image in Fig. 3.

After the extraction of the samples in Fig. 3f, the average RGB color values of each sample are obtained as

$$\boldsymbol{c}_i = \frac{1}{N_i} \sum_{j=1}^{N_i} \boldsymbol{c}_{ij}, \tag{1}$$

where N_i is the number of extracted pixels for sample i, and $\boldsymbol{c}_{ij}$ is the RGB color vector for pixel j in sample image i. The RGB color vectors are on the form

$$\boldsymbol{c}_{ij} = \left(r_{ij}, g_{ij}, b_{ij}\right), \tag{2}$$

where r_{ij}, g_{ij}, and b_{ij} are the individual red, green, and blue color intensity values (0 to 255) for pixel j in sample

image i. The differences in RGB color intensity (ΔRGB values) between a sample i and a reference sample are obtained as

$$\Delta \boldsymbol{c}_i = \boldsymbol{c}_i - \boldsymbol{c}_{\text{ref}}. \quad (3)$$

The presented algorithm is enlisted as a link in Additional file 3.

Chemometric analysis

The ΔRGB values extracted with the previously described algorithm were used for multivariant discriminant analysis. These analyses are based on 27 vectors representing a bacterial species (7 olfactory receptors and RGB values). The Hierarchical Cluster Analysis (HCA) used a "Ward" cluster method, and Linear Discriminant Analysis (LDA) was carried out in Origin(Pro), Version 2021 (OriginLab Corporation, Northampton, MA, USA). The experiment was conducted in five or six replicates per triplicate.

Abbreviations

AuNPs	Gold nanoparticles
LSPR	Localized surface plasmon resonance
HCA	Hierarchical cluster analysis
LDA	Linear discriminant analysis
TEM	Transmission electron microscopy
g	G force
nm	Nanometers

Supplementary Information

The online version contains supplementary material available at https://doi.org/10.1186/s42483-025-00323-7.

Additional file 1: Figure S1. HCA analysis of plasmonic sensor under different tested time points. **a** 30 minutes, **b** 1 hour, and **c** 2 hours after exposure to different tested plant pathogenic bacteria. **Figure S2.** Test of plasmonic sensor for differentiating between fluorescent and saprophytic bacteria. Pp: *P. savastanoi* pv. *phaseolicola* PSFR-01. Fluorescent pictures were photographed under UV light. Bacteria were grown on King´s B solid media for 4 days at 28 °C. **Figure S3.** Chemometric analysis with HCA **a** and LDA **b** for discriminating fluorescent and saprophytic bacteria. The keys Col 1, 2, and 3 refer to isolates Col1, Col2, and Col3 in Figure S2, respectively. Pp: reference strain of *P. savastanoi* pv. *phaseolicola* PSFR-01. In b "X": group mean, experiments were assessed using 6 replicates.

Additional file 2: Table S1. Parameters for the sample identification and extraction process and values for the example image in Fig. 3.

Additional file 3: Optoelectronic algorithm for image analysis and RGB extraction.

Acknowledgements

Mendoza-Figueroa and Chávez-Ramírez thanks to Sistema Nacional de Investigadoras e Investigadores (SNII) CONAHCYT and EDI-IPN.

Author contributions

MM, AA, and OJ performed experiments, WJ developed the image analysis algorithm and contributed to the manuscript writing, SJ, CJ, and CR participated in research and data analysis, CB and MS conceived and designed the experiments and wrote the manuscript.

Funding

This research was financially supported by "Proyectos de Innovación Profesores Instituto Politécnico Nacional, 2022–2023" Number 2022/6986 and 2023/1109. Saniger-Blesa J thanks to DGPA-UNAM for financial supporting in proyect PAPIIT IT100721.

Availability data and materials

Link of optoelectronic imaging analysis algorithms https://drive.google.com/file/d/1V9Qck_uJkxCdGGDJsP-4MdbLdY7TY2yH/view?usp=drive_link.

Declarations

Ethics approval and consent to participate

Not applicable.

Consent for publication

Not applicable.

Competing interests

The authors declare that they have no competing interests.

Author details

[1]Laboratorio de Protección Vegetal (Plant Protection Lab), Department of Microbiology, Escuela Nacional de Ciencias Biológicas, Instituto Politécnico Nacional (IPN), 11340 Mexico City, Mexico. [2]Laboratorio Universitario de Caracterización Espectroscópica, Instituto de Ciencias Aplicadas y Tecnología, Universidad Nacional Autónoma de México (UNAM), 04510 Mexico City, Mexico. [3]Laboratorio de Inmunomicrobiología (Immunomicrobiology Lab, Department of Microbiology, Escuela Nacional de Ciencias Biológicas, Instituto Politécnico Nacional (IPN), 11340 Mexico City, Mexico. [4]Department of Civil and Industrial Engineering, Ångströmlaboratoriet, Uppsala University, 752 37 Uppsala, Sweden. [5]Laboratorio de Fitopatología (Plant Pathology Lab), Department of Microbiology, Escuela Nacional de Ciencias Biológicas, Instituto Politécnico Nacional (IPN), 11340 Mexico City, Mexico.

Received: 15 May 2024 Accepted: 11 February 2025
Published online: 06 May 2025

References

Bai T, Sun J, Che R, et al. Controllable preparation of core–shell Au–Ag nanoshuttles with improved refractive index sensitivity and SERS activity. ACS Appl Mater Interfaces. 2014;6(5):3331–40. https://doi.org/10.1021/am405357v.

Bordbar MM, Nguyen T-A, Tran AQ, Bagheri H. Optoelectronic nose based on an origami paper sensor for selective detection of pesticide aerosols. Sci Rep. 2020a;10(1):17302. https://doi.org/10.1038/s41598-020-74509-8.

Bordbar MM, Tashkhourian J, Tavassoli A, Bahramali E, Hemmateenejad B. Ultrafast detection of infectious bacteria using optoelectronic nose based on metallic nanoparticles. Sens Actuators B Chem. 2020b;319:128262. https://doi.org/10.1016/j.snb.2020.128262.

Bueno L, Meloni GN, Reddy SM, Paixão TRLC. Use of plastic-based analytical device, smartphone and chemometric tools to discriminate amines. RSC Adv. 2015;5(26):20148–54. https://doi.org/10.1039/C5RA01822F.

Cardoso RM, Pereira TS, Facure MHM, et al. Current progress in plant pathogen detection enabled by nanomaterials-based (bio)sensors. Sens Actuators Rep. 2022;4:100068. https://doi.org/10.1016/j.snr.2021.100068.

Chen H, Kou X, Yang Z, Ni W, Wang J. Shape- and size-dependent refractive index sensitivity of gold nanoparticles. Langmuir. 2008;24(10):5233–7. https://doi.org/10.1021/la800305j.

Cheng J, Ge L, Xiong B, He Y. Investigation of pH effect on gold nanorod synthesis. J Chin Chem Soc. 2011;58(6):822–7. https://doi.org/10.1002/jccs.201190128.

Davis MJ, Gillaspie AG, Vidaver AK, Harris RW. Clavibacter: a new genus containing some phytopathogenic coryneform bacteria, including *Clavibacter xyli* subsp. *xyli* sp. nov., subsp. nov. and *Clavibacter xyli* subsp. *cynodontis* subsp. nov., pathogens that cause ratoon stunting disease of sugarcane and bermudagrass stunting disease. Int J Syst Bacteriol. 1984;34(2):107–17. https://doi.org/10.1099/00207713-34-2-107.

Duan W, Liu A, Li Q, et al. Toward ultrasensitive and fast colorimetric detection of indoor formaldehyde across the visible region using cetyltrimethylammonium chloride-capped bone-shaped gold nanorods as "chromophores." Analyst. 2019;144(15):4582–8. https://doi.org/10.1039/C9AN00694J.

Guevarra RB, Magez S, Peeters E, Chung MS, Kim KH, Radwanska M. Comprehensive genomic analysis reveals virulence factors and antibiotic resistance genes in *Pantoea agglomerans* KM1, a potential opportunistic pathogen. PLoS ONE. 2021;16(1):e0239792. https://doi.org/10.1371/journal.pone.0239792.

Krämer J, Kang R, Grimm LM, De Cola L, Picchetti P, Biedermann F. Molecular probes, chemosensors, and nanosensors for optical detection of biorelevant molecules and ions in aqueous media and biofluids. Chem Rev. 2022;122(3):3459–636. https://doi.org/10.1021/acs.chemrev.1c00746.

Li J, Wang Y, Zhang Q, et al. New application of old methods: Development of colorimetric sensor array based on Tollen's reagent for the discrimination of aldehydes based on Tollen's reagent. Anal Chim Acta. 2020;1096:138–47. https://doi.org/10.1016/j.aca.2019.10.045.

Liao C, Shi J, Zhang M, et al. Optical chemosensors for the gas phase detection of aldehydes: mechanism, material design, and application. Mater Adv. 2021;2(19):6213–45. https://doi.org/10.1039/D1MA00341K.

Ma W, Pang Z, Huang X, et al. Citrus Huanglongbing is a pathogen-triggered immune disease that can be mitigated with antioxidants and gibberellin. Nat Commun. 2022;13(1):529. https://doi.org/10.1038/s41467-022-28189-9.

Mansfield J, Genin S, Magori S, et al. Top 10 plant pathogenic bacteria in molecular plant pathology. Mol Plant Pathol. 2012;13(6):614–29. https://doi.org/10.1111/j.1364-3703.2012.00804.x.

Nazarov PA, Baleev DN, Ivanova MI, Sokolova LM, Karakozova MV. Infectious plant diseases: etiology, current status, problems and prospects in plant protection. Acta Naturae. 2020;12(3):46–59. https://doi.org/10.32607/actanaturae.11026.

Salles MO, Meloni GN, de Araujo WR, Paixão TRLC. Explosive colorimetric discrimination using a smartphone, paper device and chemometrical approach. Anal Methods. 2014;6(7):2047–52. https://doi.org/10.1039/C3AY41727A.

Sau TK, Rogach AL, Döblinger M, Feldmann J. One-step high-yield aqueous synthesis of size-tunable multispiked gold nanoparticles. Small. 2011;7(15):2188–94. https://doi.org/10.1002/smll.201100365.

Soudi M, Alimadadi N, Ghadam P. Minimal phenotypic test for simple differentiation of *Xanthomonas campestris* from other yellow-pigmented bacteria isolated from soil. Iran J Microbiol. 2011;3(2):84–91.

Tuersun P, Yusufu T, Yimiti A, Sidike A. Refractive index sensitivity analysis of gold nanoparticles. Optik (Stuttg). 2017;149:384–90. https://doi.org/10.1016/j.ijleo.2017.09.058.

Venbrux M, Crauwels S, Rediers H. Current and emerging trends in techniques for plant pathogen detection. Front Plant Sci. 2023. https://doi.org/10.3389/fpls.2023.1120968.

Wang S, Xi W, Cai F, Zhao X, Xu Z, Qian J, He S. Three-photon luminescence of gold nanorods and its applications for high contrast tissue and deep in vivo brain imaging. Theranostics. 2015;5(3):251–66.

Wang Y, Guan M, Yan X, et al. Gold nanorods assisted silver mirror reaction for consecutive color change based on-site visual semi-quantification of indoor formaldehyde. Atmos Environ. 2021;246:118101. https://doi.org/10.1016/j.atmosenv.2020.118101.

Weisskopf L, Schulz S, Garbeva P. Microbial volatile organic compounds in intra-kingdom and inter-kingdom interactions. Nat Rev Microbiol. 2021;19(6):391–404. https://doi.org/10.1038/s41579-020-00508-1.

Zhang Y, Askim JR, Zhong W, Orlean P, Suslick KS. Identification of pathogenic fungi with an optoelectronic nose. Analyst. 2014;139(8):1922–8. https://doi.org/10.1039/C3AN02112B.

Zhang Q, Li J, Wang Y, et al. Detection of aldehydes by gold nanoparticle colorimetric array based on Tollens' reagent. Anal Methods. 2021;13(45):5478–86. https://doi.org/10.1039/D1AY01431E.